RESEARCH ARTICLE

Numerical simulations of fatigue loads on wind turbines operating in wakes

Zhenqing Liu[1] 🆔 | Qiuming Li[1] | Takeshi Ishihara[2] | Jie Peng[1]

[1]Institute of Computational Wind Engineering and Wind Energy, School of Civil Engineering and Mechanics, Huazhong University of Science and Technology, Wuhan, Hubei, China

[2]Department of Civil Engineering, School of Engineering, The University of Tokyo, Tokyo, Japan

Correspondence
Zhenqing Liu, Institute of Computational Wind Engineering and Wind Energy, School of Civil Engineering and Mechanics, Huazhong University of Science and Technology, Wuhan, Hubei 410082, China.
Email: liuzhenqing@hust.edu.cn

Abstract

Wake effects increase the fatigue loads on wind turbines in operation. However, the wake flow is considerably different from the traditional boundary layer flow, and poses many challenges in determining the fatigue loads on wind turbines operating in a wake. Therefore, in the present study, the actuator-line model was adopted to numerically simulate the wake flow and an in-house code named AOWT, which is based on a generalized coordinate method, was developed for analyzing the dynamics of wind turbines under an arbitrary distribution of the turbulent flow field varying in time and space. Using the numerically modeled instantaneous wake flow fields and AOWT, the dynamic response of a wind turbine, located at specified positions in both tandem and staggered arrangements in a wake, was examined, and the fatigue loads were determined. Furthermore, to determine the major contributions to the fatigue loads, the loads induced by the spatial variation of the mean flow fields were predicted. To the best of the authors' knowledge, no such analysis has been conducted thus far. Importantly, it was found that in the near-wake region, the mean flow field had a significant influence on the fatigue loads, especially in the staggered layout. However, there is no analytical wake model available in the literature capable of predicting the near-wake mean flow fields. Therefore, in this study, a near-wake model was proposed, which yielded satisfactory predictions of the mean velocities in the near-wake region.

KEYWORDS

blade element method, dynamic response, fatigue load, LES, wake flow, wake model

1 | INTRODUCTION

Wind turbines are usually installed as wind farms, in which the upstream wind turbines disturb the upcoming flow field and increase the downstream turbulence.[1-7] Consequently, the fatigue loads on the downstream wind turbines owing to the wake effects are different from those created by a traditional boundary layer flow.[8,9]

A method using the effective turbulence intensity[10,11] has been commonly employed to assess the wake effects on the fatigue loads on wind turbines. However, the flow field in a wake is strongly distorted in terms of both the turbulence intensity and the mean flow. As a result, detailed examinations of the wake effects on the fatigue loads are needed. Whereas, the researches[12-15] considering this issue are not as many as those about the fatigue loads induced by the traditional boundary layer.[16-20] This could be owing to the fact that the wind turbine wake flow is much different with the traditional boundary layer flow, failing the applications of the conventional approaches for the turbulent flow generations,[11,21] posing many challenges in determining the fatigue loads on a wind turbine operating in wakes. In recent years, the engineering models, such as

the dynamic wake meandering (DWM) model,[22-24] which is integrated in HAWC2[25] and FAST.Farm,[26] are intended to be used to estimate the fatigue of turbines in wake.

Wind turbines operating in wakes were first studied by Thomsen and Sørensen.[12] It was found that the most important parameters determining the fatigue load are the turbulence intensity and the length scale of the wind. Next, Lee et al[13] investigated the wake effects on wind turbines with a tandem arrangement, and concluded that the wakes from the upstream turbines had a significant impact. However, the distance between the downstream and upstream wind turbines in that study was a constant. The examination about the relative locations of the wind turbines operating in the wake was limited. Furthermore, Kim et al[14] examined the wake effects on the fatigue loads and found that the additional turbulence intensity significantly increased the fatigue loads. However, the time histories of the wake flow fields acting on the downstream wind turbines were generated using the traditional analytical method, and hence were different from the real wake flows. Recently, Meng et al[15] developed an elastic actuator line model (ALM) to simulate the dynamic responses of wind turbines in the wake. Two staggered turbines in a neutral atmospheric condition were examined and it was found that the downstream wind turbine suffered higher fatigue loads than the upstream one. However, the developed elastic actuator line model did not consider the effect of the coupling between the blades and tower, which is significant for the dynamic responses of wind turbines.[27] In addition, the relative importance of the spatial variation of the mean flow field and that of the turbulence for the fatigue loads on wind turbines was not clarified.

To predict the wake-induced fatigue loads on wind turbines, it is critical to identify a satisfactory analytical model for the wake flow. One of the widely used wake models for velocity deficit was proposed by Jensen[28] and was further developed by Katic et al.[29] This assumed a linearly expanding wake with a uniform profile for the velocity deficit. Then, Frandsen et al[30] proposed a model that applied the momentum balance, in addition to the mass conservation. The velocity deficit was still assumed to be uniform in their model. Subsequently, a Gaussian distribution of the velocity deficit was derived by Ishihara et al[31] and observed in experiments by Ishihara et al[31] and Chamorro and Porte-Agel.[6] This Gaussian distribution was also employed in the analytical models by Bastankhah and Porte-Agel[32] and Gao et al.[33] However, there is still no model capable of accurately predicting the flow field in the near-wake region. Such a model is probably very crucial to determine the wake-induced fatigue loads in some wind farms, where the distance between the wind turbines is approximately twice as large as the rotor diameter, D, such as in the Nanao Eastern Island wind farm in Shantou, Guangdong, China, as depicted in Figure 1. This type of wind farms can be commonly observed on islands in Taiwan Strait, famous for their rich wind energy resources.

Therefore, the present study has two objectives in the present study: (a) to understand the fatigue loads on wind turbines operating in wakes, and (b) to propose a near-wake analytical model. To realize these two objectives, the ALM is adopted to simulate the wake flow field numerically. Then, an in-house code named "Analysis tool of On-shore Wind Turbines (AOWT)", based on a generalized coordinate method, is developed to calculate the dynamics of wind turbines under an arbitrary distribution of flow field varying in both space and time. Next, the fatigue loads on a wind turbine operating in a wake are examined in detail. Finally, based on the model proposed by Ishihara and Qian,[34] an analytical near-wake flow field model is proposed.

2 | WIND TURBINE WAKE SIMULATION

2.1 | Governing equations

Large eddy simulation (LES) is adopted, in which the large eddies are directly computed, while the influence of eddies smaller than the grid spacing is parameterized. To close the cell-space averaged Navier-Stokes (N-S) equations, a subgrid scale (SGS) model is adopted. Following the previous studies, for example, the one by Ishihara and Qian,[34] the standard Smagorinsky-Lilly SGS model[35] is applied. The governing equations obtained by filtering the N-S equations are expressed as:
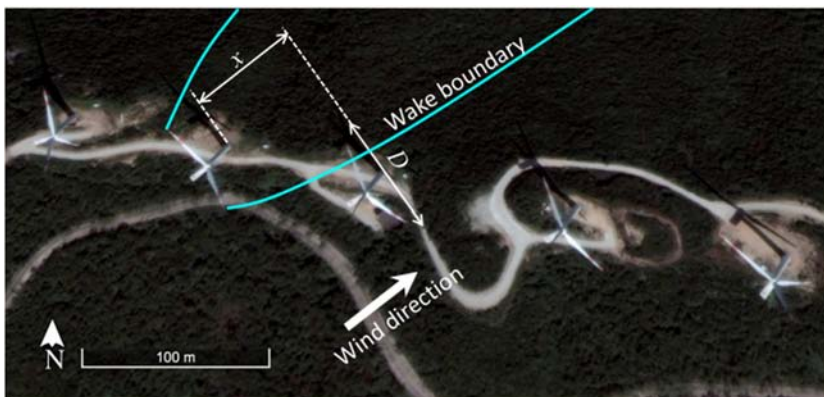

FIGURE 1   Nanao eastern island wind farm in Shantou, Guangdong, China [Colour figure can be viewed at wileyonlinelibrary.com]

$$\frac{\partial \rho}{\partial t} + \frac{\partial}{\partial x_i}(\rho \tilde{u}_i) = 0, \tag{1}$$

$$\frac{\partial \tilde{u}_i}{\partial t} + \frac{\partial \tilde{u}_i \tilde{u}_j}{\partial x_j} = -\frac{1}{\rho}\frac{\partial \tilde{p}}{\partial x_i} + \mu \frac{\partial}{\partial x_j}\left(\frac{\partial \tilde{u}_i}{\partial x_j}\right) + \frac{\partial \tilde{\tau}_{ij}}{\partial x_j} + f_i, \tag{2}$$

where, ρ denotes the density, $\tilde{p}$ is the fitted pressure, $\tilde{u}_i$ represents the fitted velocities ($\tilde{u}$, $\tilde{v}$, $\tilde{w}$), μ is the viscosity, $\tilde{\tau}_{ij}$ denotes the SGS stress, and f_i is the source term representing the external force because of the effects of the wind turbine, which is determined by ALM.[36,37] In the present LES, the Gaussian smearing technology[38,39] capable of improving the accuracy and the stability of the simulation when using ALM was not applied. But the comparison between the present numerical simulation and the experiment is good as presented below. In the near future, we will try to realize the Gaussian smearing technology in the code.

In the Smagorinsky-Lilly model, the SGS stress is parameterized as:

$$\tau_{ij} = \mu_t\left(\frac{\partial \tilde{u}_i}{\partial x_j} + \frac{\partial \tilde{u}_j}{\partial x_i}\right) = -2\mu_t \tilde{S}_{ij} + \frac{1}{3}\tau_{kk}\delta_{ij} \tag{3}$$

$$\tilde{S}_{ij} = \frac{1}{2}\left(\frac{\partial \tilde{u}_i}{\partial x_j} + \frac{\partial \tilde{u}_j}{\partial x_i}\right) \tag{4}$$

in which, $\tilde{S}_{ij}$ is the rate-of-strain tensor for the resolved scale, δ_{ij} is the Kronecker delta, and μ_t denotes the SGS turbulent viscosity force and is defined as:

$$\mu_t = \rho L_s^2 \left|\tilde{S}\right| = \rho L_s^2 \sqrt{2\tilde{S}_{ij}\tilde{S}_{ij}} \tag{5}$$

$$L_s = \min\left(\kappa d, C_s \Lambda^{\frac{1}{3}}\right) \tag{6}$$

where, L_s denotes the mixing length of the SGS, κ is the von Kármán constant (0.42), d represents the distance to the closest wall, and Λ is the volume of a computational cell. C_s is the Smagorinsky constant and is determined according to the study by Ishihara and Qian[34] to be 0.032.

2.2 | Wind turbine

A 1:100 scaled Mitsubishi's MWt-1000 wind turbine[34] is used in this study. The rotor diameter of the scaled model, D, is 0.57 m, and the hub height is 0.7 m. The rated wind speed of this wind turbine, U_r, is 10 m s^{-1}. Ishihara et al[31] carried out wind tunnel experiments and the flow fields in the wake of the wind turbine were obtained. In that experiment, four cases were examined with two different tip speed ratios (λ = 5.52 and 9.69) and two different inflow turbulence intensities (I_a = 0.035 and 0.137).

Considering the fact that the tip speed ratio of this wind turbine in operation is approximately 10.0 and the turbulence intensity is always in the range of 0.1 to 0.2 based on the guidelines, such as IEC 3rd edition[11] and Germanischer Lloyd rules (GL, 1993),[40] a case with λ = 9.69 and I_a = 0.137 is finally selected to be examined in the present study.

In this case, the corresponding pitch angle equals 0 and the thrust force coefficient, C_T, equals 0.81. The wind speed at the hub height, U_h, in the experiments is 10.2 m s^{-1}. The Reynolds number is determined as $\rho U_h H_{hub}/\mu$, which equals to 4.8×10^5 for the scaled model. The key parameters of the wind turbine are listed in Table 1. More details of this scaled wind turbine can be found in the study by Ishihara and Qian[34] and are not repeated here so as to focus more on the results.

TABLE 1 Key parameters of the wind turbine

Wind Turbine Type	Tip Speed Ratio, λ	Thrust Force Coefficient, C_T	Pitch Angle, (°)	Rated Wind Speed, U_r, m s^{-1}	Rotor Diameter, D (m)	Hub Height, H_{hub}(m)	Reynolds Number in Scale, $\rho U_h H_{hub}/\mu$
Mitsubishi		MWt-1000	9.69	0.81	0	10	57
70	4.8×10^5						

2.3 | Computational domain and solution methods

The numerical simulations were performed in a modeled traditional boundary layer, which was generated by three spires and a fence, as illustrated in Figure 2. This arrangement is the same as that used by Ishihara et al[31] in their experiments. The length, height, and width of the computational domain were 15.5, 1.8, and 1.5 m, respectively. The wind turbine was located 8.0 m downstream of the inlet and the tower base center was the origin of this domain ($x = 0$, $y = 0$, $z = 0$), where x, y, and z are coordinates in the streamwise, spanwise, and vertical directions, respectively. The three spires were arranged 6.0 m upstream of the wind turbine, and the fence was located 5.5 m upstream of the wind turbine. The rotor disk was divided in a uniform distance of 0.01 m and then connected smoothly with the main domain. The main domain was divided by a set of rectangular cells with minimum grid size of 0.001 m near the wall in vertical direction and 0.02 m in horizontal direction. The total grid number is 7.2×10^6.

At the inlet, a uniform velocity of 10 m s^{-1} was prescribed as the inlet boundary condition, ie, $\bar{u} = 10$ m s^{-1} and $\partial \bar{p}/\partial n = 0$. At the outlet, the pressure-outlet condition was specified, ie, $\bar{p} = 0$ and $\partial \bar{p}/\partial n = \partial \bar{u}_i/\partial n = 0$. Furthermore, the symmetry conditions were applied at the top and the sides of the computational domain, ie, $\partial \bar{u}/\partial n = \partial \bar{v}/\partial n = \partial \bar{p}/\partial n = 0$. In addition, the wall boundary conditions were used at the other boundaries, ie, $\partial \bar{p}/\partial n = 0$ and $\bar{u}_i = 0$. Table 2 summarizes the settings for the boundary conditions.

The finite volume method (FVM) was used for the simulations, wherein the variables were distributed in a nonstaggered, cell-centered mesh system. The second-order central difference scheme was used for the convective and viscous terms. In addition, the second-order implicit scheme was used for the unsteady term.

The semi-implicit pressure-linked equations (SIMPLE) algorithm, which was introduced by Ferziger and Peric,[41] was used to solve the discretized equations. The commercial software Fluent 14.0 was used for the calculations. A time step size Δt of 0.0001 seconds was used. The simulation lasted for 30 seconds and the first 10 seconds of the transient results were discarded. The following 20 seconds of the results were used for the statistical analysis.

2.4 | Flow field and validation

Figure 3 depicts the distributions of the mean streamwise velocity, U, and the streamwise fluctuation, σ_u. Figure 3A,B shows these variables in the absence of the wind turbine (abbreviated as "free flow"), whereas Figure 3C,D shows the same variables after the introduction of the wind turbine
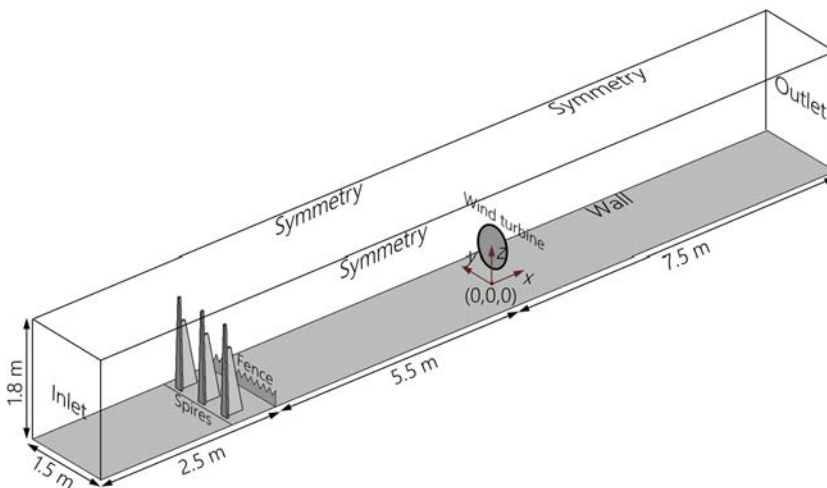

FIGURE 2 Schematic of the computational domain [Colour figure can be viewed at wileyonlinelibrary.com]

TABLE 2 Settings for the boundary conditions

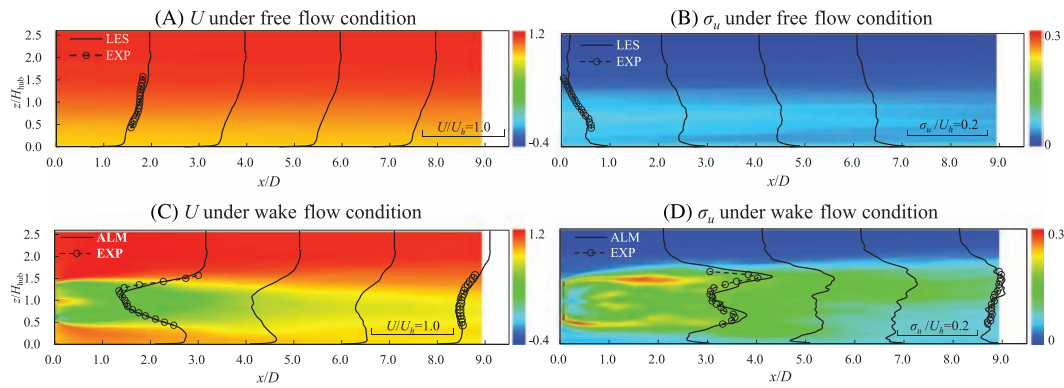| Locations	Boundary Type	Expression
Inlet	Velocity inlet	$\bar{u} = 10$ m/s, $\partial \bar{p}/\partial n = 0$
Spires and fence	Non-slip wall	$\partial \bar{p}/\partial n = 0$, $\bar{u}_i = 0$
Bottom	Non-slip wall	$\partial \bar{p}/\partial n = 0$, $\bar{u}_i = 0$
Side walls and tope of the domain	Symmetry	$\partial \bar{u}/\partial n = \partial \bar{v}/\partial n = \partial \bar{p}/\partial n = 0$
Outlet	Pressure-outlet	$\bar{p} = 0$, $\partial \bar{u}_i/\partial n = 0$

FIGURE 3 Mean streamwise velocities and the fluctuations under (A,B) the free-flow condition and (C,D) the wake flow condition [Colour figure can be viewed at wileyonlinelibrary.com]

(abbreviated as "wake flow"). In these figures, the profiles obtained from the wind tunnel experiments conducted by Ishihara et al[31] are superimposed for comparison purposes. It can be seen that there is a satisfactory agreement between the two results. It is evident that the wind turbine significantly decreased the wind speed in the near-wake region, where the increase in the fluctuations was also obvious at locations with approximately the same height as the blade tip. More details of the validation of the modeled flow fields in the wake of wind turbine can be found in the study by Ishihara and Qian.[34]

The instantaneous flow fields under both free flow and wake flow conditions were recorded from 10 to 30 seconds at each time step during the simulation. For the flow field under the free-flow condition, owing to the fully developed turbulence, the data at the cell centers on the spanwise slice ($x = 0$) were extracted. On the other hand, for the wake flow condition, the data at the cell centers on the span-wise slices, ie, $x = 2D$, $4D$, $6D$, and $8D$ were extracted. Next, the coordinates of the cell centers as well as the time were divided by the scale of the model, which was 1:100. Considering that the rated wind speed of this wind turbine was 10 m s^{-1}, which was approximately equivalent to $U_h = 10.2$ m s^{-1} in the simulation, the wind speed in the simulation was therefore not scaled. Thus, the flow fields at full scale on these slices were obtained and used to determine the aerodynamic loads on the blades and the tower of the wind turbines, under both free-flow and wake flow conditions, at different downstream locations. These are described in detail in Section 4.

3 | INTRODUCTION TO AOWT

For the calculation of the dynamic response of wind turbines, the degrees of freedoms (DOFs) are considerably large when the traditional finite element method (FEM)[42] is used, which entails a high computational cost. Furthermore, most aeroelastic tool, such as the widely used commercial software GH-bladed,[43] can take a turbulence box as input, which is a prescribed varying flow field. However, as far as we know, in the turbulence box only the wind properties along the vertical direction can be specified. The variation of the wind properties in the lateral direction can hardly be considered. For example, the integral length of the velocity, the turbulence intensity, the mean velocity, and the spectrum of the velocity is assumed to be constants at a certain height. Then, adopting some mathematical methods, such as superposition harmonic method,[44,45] the wind with turbulence can be generated. However, in the wake of the wind turbine, the integral length of the velocity, the turbulence intensity, the mean velocity, and the spectrum of the velocity varies not only in the vertical direction but also in the lateral direction. Therefore, the turbulence box cannot generate such complex wake flow. This is one of the motivations for us to develop the solver AOWT. Therefore, in the present study, a code capable of inputting arbitrary distributions of the turbulent flow fields varying in space and time is developed. This code was registered as "Analysis tool of On-shore Wind Turbines (AOWT)" in the National Copyright Administration of the People's Republic of China. AOWT adopts the generalized coordinate approach,[46,47] which is also applied in the popular tools in the wind energy community OpenFAST[48] and FLEX.[49] The details of the governing equations for the dynamic response of the wind turbines can be obtained from the studies conducted by Zhang.[46,47]

3.1 | Calculation details

The aerodynamic loads were determined using the blade element method (BEM).[50] The fluid-structure interaction (FSI) was not taken into account because of the considerably small speed produced by the structural vibration (less than 1.0 m s^{-1}), compared with the inflow wind speed (approximately equal to 10 m s^{-1}). The Newmark-β method was adopted to advance the calculation in time. The time-step size in the calculation of the structural dynamic response was 0.01 seconds. For each run of the calculation, the first 60 seconds of transient data were discarded and

the resulting stable results were applied for further processing. It should be pointed out that as the inputs of AOWT, the modal shapes could be determined beforehand. In the present study, the first three flapwise modes for the blade, the first three edgewise modes for the blade, the first three fore-aft modes for the tower, and the first three lateral modes for the tower were applied to do the calculations, and to limit the differences with GH-bladed, the modal shapes calculated using GH-bladed were directly adopted. The natural frequencies for both the blade and the tower are listed in Table 3. In the following study, the flapwise bending moments, M_{y3} at the blade root, and the fore-aft bending moments, M_{y1} at the tower base, which were the components that were most sensitive to the variations of the flow field, were examined.

3.2 | Validation of AOWT

The dynamic response of a wind turbine in a traditional boundary layer flow was calculated using GH-bladed and AOWT. The turbulent flow fields in this validation case was generated by GH-bladed, with a wind profile of $U = 10(z/H_{hub})^{0.2}$ m s^{-1} and a turbulence intensity of $I_a = 0.33$. The results from these two codes were comparable, exhibiting almost the same peak values at almost the same time, as illustrated in Figure 4. The maximum discrepancy was approximately only 5%, thus validating the accuracy of AOWT.

It should be pointed out that in the present version of AOWT, the geometrical nonlinearities and the axial deformation effects were not included. This is from the consideration that the modeled wind turbine in the present study is with a relatively small size, the effects from the geometrical nonlinearities and the axial deformation were not evident. Neglecting the geometrical nonlinearities and axial deformation effects will result in some inaccuracies, which can be found from the above validation of AOWT. The maximum error was about 5%, which is however small enough and we think the result from AOWT can be adopted for the further examination of the fatigue loads. With the increase of the size of the wind turbine, the geometrical nonlinearities effect will be more evident, so the geometrical nonlinearities and the axial deformation effects will be considered in the next version of AOWT.

TABLE 3 Natural frequencies of the blade and the tower

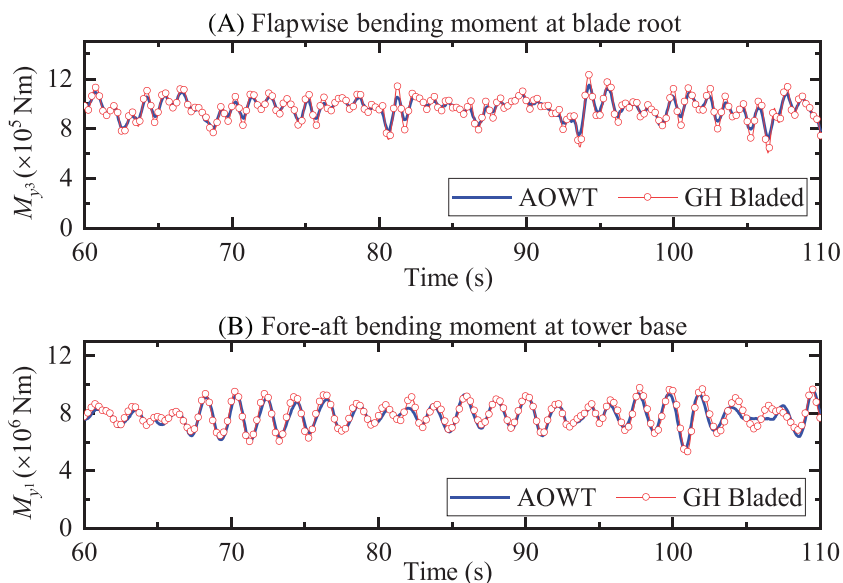| Mode	Frequency of Blade, Hz	Mode	Frequency of Tower, Hz
First edgewise mode	1.161	First lateral mode	0.492
Second edgewise mode	3.976	Second lateral mode	3.879
Third edgewise mode	9.081	Third lateral mode	11.07
First flapwise mode	0.753	First fore-aft mode	0.492
Second flapwise mode	2.273	Second fore-aft mode	3.879
Third flapwise mode	4.949	Third fore-aft mode	11.14

FIGURE 4 Validation of (A) the flapwise bending momentums at the blade root and (B) the fore-aft bending momentums at the tower base [Colour figure can be viewed at wileyonlinelibrary.com]

4 | WAKE-INDUCED FATIGUE LOAD

4.1 | Case settings

The downstream wind turbine was placed at eight different locations in consecutive analyses, with four tandem arrangements and four staggered arrangements. The distances from the downstream turbine to the upstream turbine in each of the two types of arrangements were 2*D*, 4*D*, 6*D*, and 8*D*. In the staggered arrangement, the downstream turbine was located at a spanwise distance of 0.5*D* from the wake center, as depicted in Figure 5. Table 4 summarizes the case settings.

4.2 | Time histories and statistics

Figures 6 and 7 depict the time histories of the moments at the blade root and the tower base. Owing to the deficit of wind speed in the wake, the averaged bending moments were much lower than those caused by the free flow. However, the moment fluctuations became extraordinarily large, and could be attributed to the strong wind shear and the large turbulence caused by the upstream wind turbine. When the wind turbine

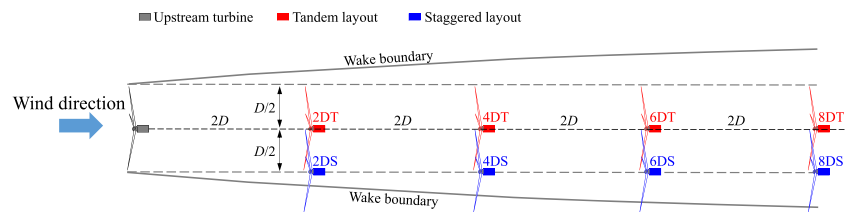**FIGURE 5** Layout of the wind turbines [Colour figure can be viewed at wileyonlinelibrary. com]

TABLE 4 Cases settings

Cases	Distance	Layout	Condition
Free	/	/	○
2DT	2*D*	Tandem	
2DS	2*D*	Staggered	
4DT	4*D*	Tandem	
4DS	4*D*	Staggered	
6DT	6*D*	Tandem	
6DS	6*D*	Staggered	
8DT	8*D*	Tandem	
8DS	8*D*	Staggered	

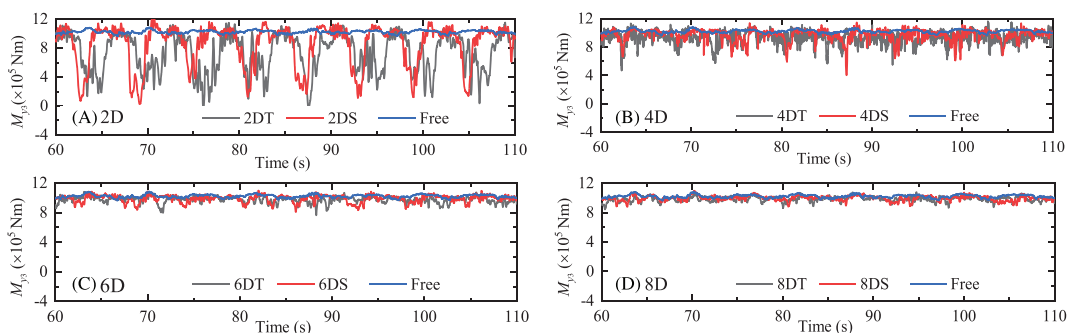*Note.* means wake flow, ○ means free flow.

FIGURE 6 Time histories of flapwise bending moment at the blade root when the wind turbine is located at (A) *x* = 2*D*, (B) *x* = 4*D*, (C) *x* = 6*D*, and (D) *x* = 8*D* [Colour figure can be viewed at wileyonlinelibrary.com]

FIGURE 7 Time histories of fore-aft bending moment at the tower base when the wind turbine is located at (A) $x = 2D$, (B) $x = 4D$, (C) $x = 6D$, and (D) $x = 8D$ [Colour figure can be viewed at wileyonlinelibrary.com]
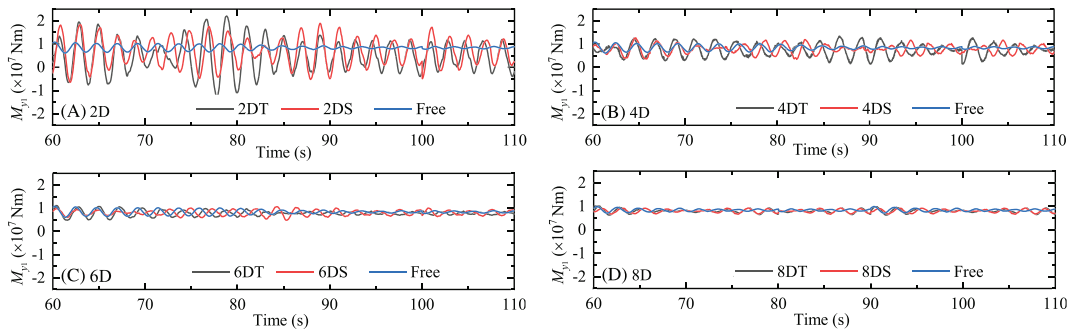
was moved downstream, the fluctuations of the moment were weakened, and at $x = 8D$, the difference between the fluctuations caused by the wake flow and the free flow could hardly be identified.

Figure 8 presents the box plots for the time series of the moment, which were normalized by the mean bending moment of the wind turbine in the free flow. The abbreviation IQR in Figure 8 stands for interquartile range. It is clear that the averaged bending moments were the smallest at $2D$ and increase as the downstream distance was increased. In addition, it is interesting to note that in general, the wind turbine in the tandem layouts, for each downstream location, experienced smaller mean bending moments than in the corresponding staggered layout case. This was because of the stronger wind deficit near the wake center. Furthermore, in the near-wake region, ie, $x = 2D$, the fluctuations of the bending moments at the blade root, when the wind turbine was in any of the tandem arrangements, were larger than those in the corresponding staggered layout case. This was probably because the blade of the wind turbine in a tandem layout was more likely to meet the flow with high turbulence and in the tandem layout the contribution from the turbulence was more dominant than that from the spatial variation of the mean wind speed. These observations will be further confirmed in the following discussion on the relative importance of the mean flow and the turbulence-induced fatigue loads. Similar trend could be observed for the bending moments at the tower base. It is also important to note that the bending moments at the blade root were more sensitive to the wake-induced flow field than the tower, as can be found from Figure 8A, in which in the far-wake region, ie, $x = 8D$, the IQR range was still about two times as large as that from the free flow. However, from Figure 8B, it is evident that the IQR ranges under the wake flow and free flow conditions became nearly the same at $x = 8D$. This could be because the vibrations of the blades could hardly be in the same phase, which would partially cancel out the wake effects of the tower.

Using the rainflow-counting algorithm,[51] the moment amplitude cycles were calculated. Figures 9 and 10 illustrate the exceedance probabilities of the bending moment amplitudes at the blade root and the tower base, respectively. At $x = 2D$, the bending-moment amplitudes under the wake flow condition showed much larger values than those under the free flow condition. In addition, the results of the wind turbine in the tandem layout were larger than those of the staggered layout. This trend continued to hold at $x = 4D$. However, at $x = 6D$ and $8D$, the results for the wind turbine in the tandem layout and the staggered layout were almost the same. For the tower base, the bending-moment amplitudes at $x = 8D$ did not show distinct differences with those under the free flow condition.
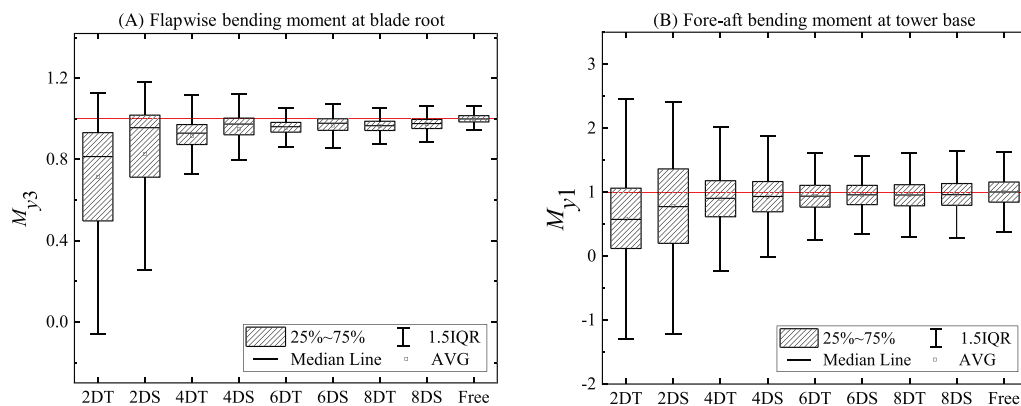

FIGURE 8 Boxplots of the time histories of the bending moment at (A) blade root and (B) tower base [Colour figure can be viewed at wileyonlinelibrary.com]
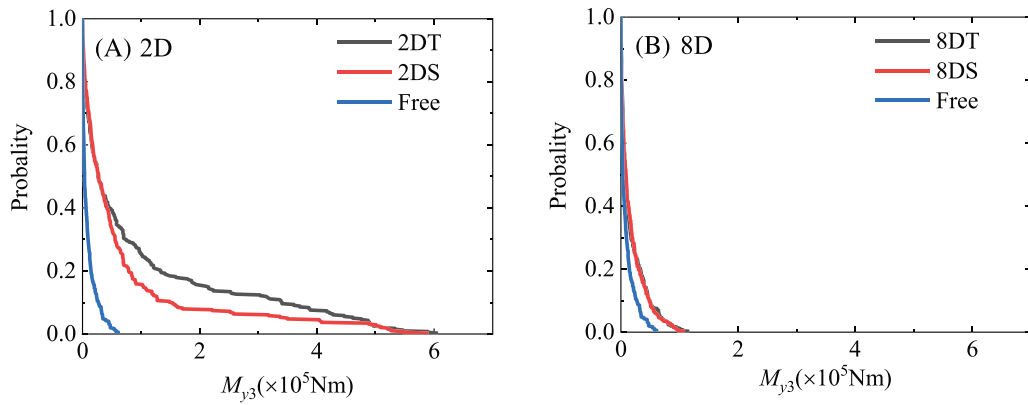
FIGURE 9   Exceedance probability of M_{y3} amplitude at the blade root by rainflow cycle counting when the wind turbine is located at (A) $x = 2D$ and (B) $x = 8D$ [Colour figure can be viewed at wileyonlinelibrary.com]

FIGURE 10   Exceedance probability of M_{y1} amplitude at the tower base by rain flow cycle counting when the wind turbine is located at (A) $x = 2D$ and (B) $x = 8D$ [Colour figure can be viewed at wileyonlinelibrary.com]
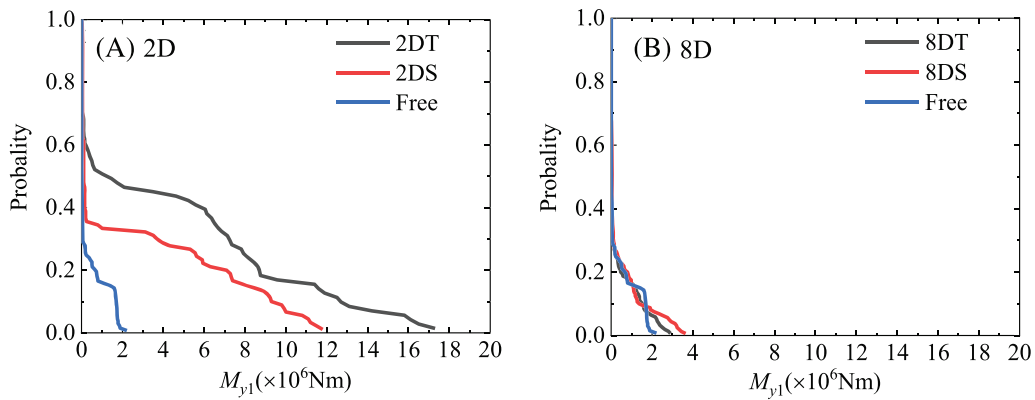
4.3 | Equivalent fatigue loads

The equivalent fatigue loads (EFL) are used to equate the fatigue damage represented by the rain flow cycle counted data to that caused by a single load range repeating at a single frequency. The EFL is given by the following formula:

$$L_N = \sqrt[l]{\frac{\sum L_i^l n_i}{N_t}}, \qquad (7)$$

where L_N is the EFL for N_t cycles; N_t is the number of cycles, which is assumed to be 1.0×10^7; L_i is the load in the range bin i; n_i is the number of rain flow cycles at the load range bin i; and l denotes the slope of the S-N curve for blades $l = 10$ and for tower $l = 5$.[52]

Figure 11 depicts the out-of-plane EFLs, where it is clear that the EFLs at $x = 2D$ were 10 times as large as those under the free flow condition. As the distance between the upstream and downstream wind turbines increased, the EFLs decreased dramatically and showed stable values when $x \geq 6D$. However, even in the far-wake region, ie, $x = 8D$, the results under the free flow condition were still significantly smaller than those under the wake flow condition. Therefore, it is important that more attention should be paid when the wind turbines are arranged with a distance of less than $8D$ between them. Even the wake flow condition did not occur as frequently as it did in the free flow condition. The EFLs under the wake flow condition night still contribute significantly to the total EFLs over the lifetime of the wind-turbine.

As mentioned above, the large EFLs under the wake flow condition resulted from two factors: the large spatial variation of the mean flow field and the large turbulence. It is of interest to understand the amount of contribution made by each of these factors. Hence, a spatially varying mean flow field was adopted, and considering the rotor rotation, the aerodynamic loads on the blades in time were determined. As a result, the EFLs caused by the mean flow field were calculated. The steps determining the fatigue load because of the spatial variation of the mean flow fields are as follows:
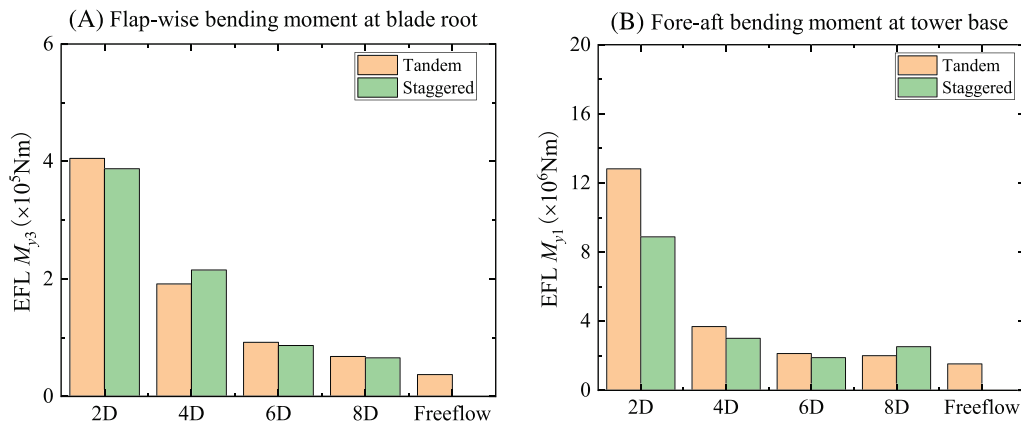
FIGURE 11 Equivalent fatigue loads at (A) the blade root and (B) the tower base, induced by the instantaneous flow fields [Colour figure can be viewed at wileyonlinelibrary.com]

- obtain the spatial distributions of the mean velocities by averaging the instantaneous velocities in time.
- Store the spatial distributions of mean velocities in a 400×400 grid with a step size of $0.01D$.
- Determine the mean velocities at the location of each blade element and at each time step through linear interpolation.
- Use BEM to determine the aerodynamic loads caused by the spatial variation of the mean flow fields.
- Calculate the dynamic response by AOWT.
- Calculate the equivalent fatigue loads using Equation (7).

The EFLs because of the mean flow fields are as shown in Figure 12. Similar to the EFLs determined by the instantaneous flow field, the EFLs determined by the mean flow field also exhibited extremely large values in the near-wake region owing to the strong spatial variations of the mean flow. Furthermore, an interesting observation is that the results in the staggered layout cases were larger than those in the tandem layout cases. This was because the wind turbine with a staggered layout was abruptly placed at the location with the largest wind shear. However, because of the expansion of the wake and the weakening of the wind deficit as the distance between the wind turbines increased, the difference between the tandem layout and the staggered layout became less obvious.

The proportion of the contribution to the EFLs from the mean flow field is plotted in Figure 13. It is obvious that in the near-wake region, ie, $x = 2D$, the turbulence was dominant in the tandem layout cases, while the mean flow contribution was dominant in the staggered layout cases, reaching about 85%. However, the mean flow contribution dramatically decreased as the distance between the wind turbines increased. When the distance was further increased, the contribution from the mean flow field generally increased, and at $x = 8D$, reached nearly the same level as the free flow condition.
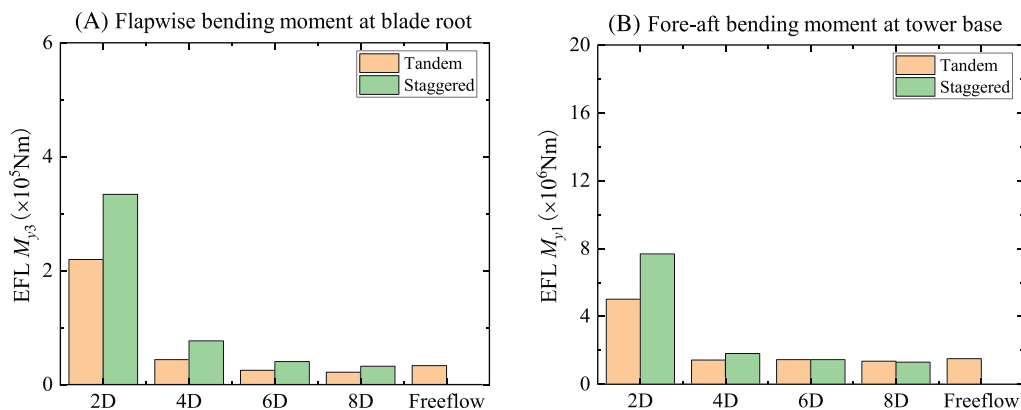

FIGURE 12 Equivalent fatigue loads at (A) the blade root and (B) the tower base, induced by the space variation of the mean flow fields [Colour figure can be viewed at wileyonlinelibrary.com]
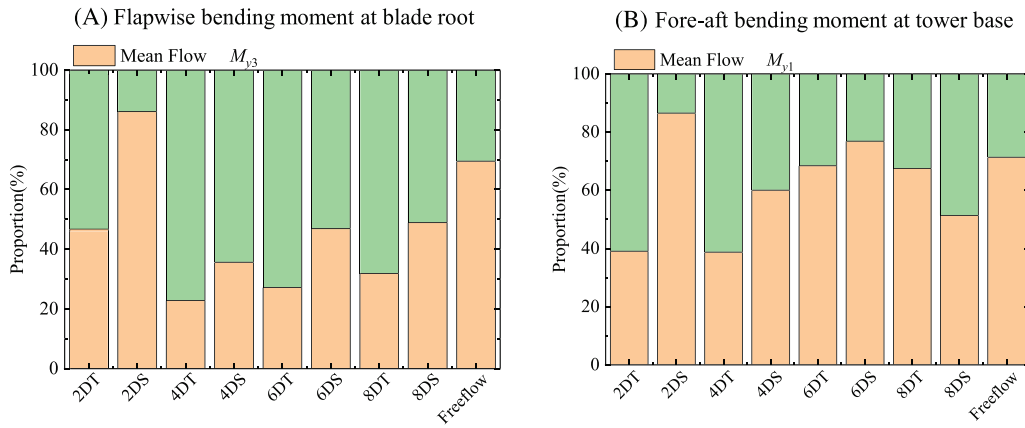
FIGURE 13 Proportion of the fatigue load at (A) the blade root and (B) the tower base, because of the space variation of the mean flow fields [Colour figure can be viewed at wileyonlinelibrary.com]

5 | PROPOSED ANALYTICAL NEAR-WAKE MODEL

From the examination about the fatigue loads, it is found that in the near-wake region, the fatigue load due to the spatial variation of the mean velocity is significant and can contribute about 85% of the total fatigue load. In addition, the near-wake fatigue load is the largest, which means that if we want to predict the fatigue load caused by the wind turbine–wake using flow fields modeled by the analytical wake model, the accurate prediction of the mean flow fields in the near-wake region is crucial. This is the motivation of the proposal of the dual Gaussian model in the present study. The model proposed in the present study is based on that by Ishihara and Qian.[34]

5.1 | Velocity deficit

The analytical model proposed by Ishihara and Qian[34] yielded satisfactory agreements with experiments and simulations at the locations $x > 4D$. However, the single Gaussian model used in that study could not fit the data satisfactorily in the near-wake region. Therefore, in the present study, a dual-Gaussian model is proposed. Similar to the wake model proposed by Ishihara and Qian,[34] in the present study, the streamwise velocity deficit is also assumed to be axisymmetric with respect to the rotor axis. However, the self-similar distribution in the wake cross-section is assumed to consist of two Gaussian functions under the consideration that the streamwise velocity deficit is strongest at the wake boundary in the near-wake region:

$$\frac{\triangle U(x,y,z)}{U_h} = \frac{1}{\left(a + b \cdot \frac{x}{D} + c\left(1 + \frac{x}{D}\right)^{-2}\right)^2}\left(k_1 \times \exp\left(-\frac{(r-m)^2}{1.75\sigma^2}\right) + k_1 \times \exp\left(-\frac{(r+m)^2}{1.75\sigma^2}\right)\right),$$

(8)

where a, b, and c are the functions of C_T and I_a, by fitting the data from experiments or simulations, m indicates the distance between the peak locations of the Gaussian function and the wake center, which should be decreased with increasing the downstream distance, x, due to the turbulence mixing effects in the wake. And m should be nearly zero in the far-wake region. σ is the representative wake width, which is assumed to expand linearly in the wake region downstream of the turbine. Considering that the mixing effects in the wake will be definitely strengthened with increasing the turbulence in the wake, which is proportional to the thrust force coefficient, C_T, and the inflow turbulence intensity, I_a, therefore, m is assumed to be as follows:

$$m = a_1 \left(\frac{x}{D}\right)^{-b_1} C_T^{-c_1} I_a^{-d_1},$$

(9)

where a_1, b_1, c_1, and d_1 are the constants with positive values. In addition, k_1 in Equation (8) is the contribution parameter of the two Gaussian functions that should decrease as increasing x, and in order to make the present model be identical with the original model by Ishihara and Qian[34] in the far-wake region, k_1 should equal 0.5 in the far wake. As a result, k_1 can be expressed as:

$$k_1 = e_1 x^{-f_1}. \tag{10}$$

The numerical and the experimental data in the study by Ishihara and Qian[34] and the studies by Wu and Porte-Agel[53,54] are adopted to fit the parameters. Finally, $a_1 = 0.453$, $b_1 = 2.0$, $c_1 = 0.1$, $d_1 = 0.1$, $e_1 = 0.89$, and $f_1 = 0.25$ are obtained. It should be pointed out that k_1 is meaningful only in the range $2D \leq x \leq 10D$. This range should be able to cover most of the cases in the wind farms. The model is listed in Table 5 for convenience. For the turbulence intensity, I, the original model by Ishihara and Qian[34] has provided satisfactory results in both the near-wake and far-wake regions, therefore, no modifications are needed for I.

5.2 | Comparisons and validations

The comparisons of the mean streamwise velocities from the LES by Ishihara and Qian,[34] single Gaussian model by Ishihara and Qian,[34] and current proposed wake model, in vertical and horizontal directions, are depicted in Figures 14 and 15, respectively. It can be seen that the wake models from the present study and that by Ishihara and Qian[34] show satisfactory agreements with the LES results in the far-wake region. However, the model by Ishihara and Qian[34] in the near-wake region overestimates the streamwise velocity at the wake boundary; however, it underestimates the same at the wake center. After modifying the model using the dual-Gaussian functions, the prediction is significantly improved in the near-wake region. The quantitative examination of the improvements of the modified analytical model is carried out based on the relative errors determined as follows:

$$\epsilon_{I\&Q} = \frac{\sum_{n=1}^{n=N} |U_{I\&Q} - U_{LES}|}{\sum_{n=1}^{n=N} |U_{LES}|}, \quad \epsilon_M = \frac{\sum_{n=1}^{n=N} |U_M - U_{LES}|}{\sum_{n=1}^{n=N} |U_{LES}|}, \tag{11}$$

where $\epsilon_{I\&Q}$ and ϵ_M are the relative errors from the model by Ishihara and Qian[34] and the proposed model, respectively, $U_{I\&Q}$ is the predicted velocity from the analytical model by Ishihara and Qian,[34] U_M is the predicted velocity from the analytical model proposed in the present study,

TABLE 5 Modification of the model by Ishihara and Qian[34]

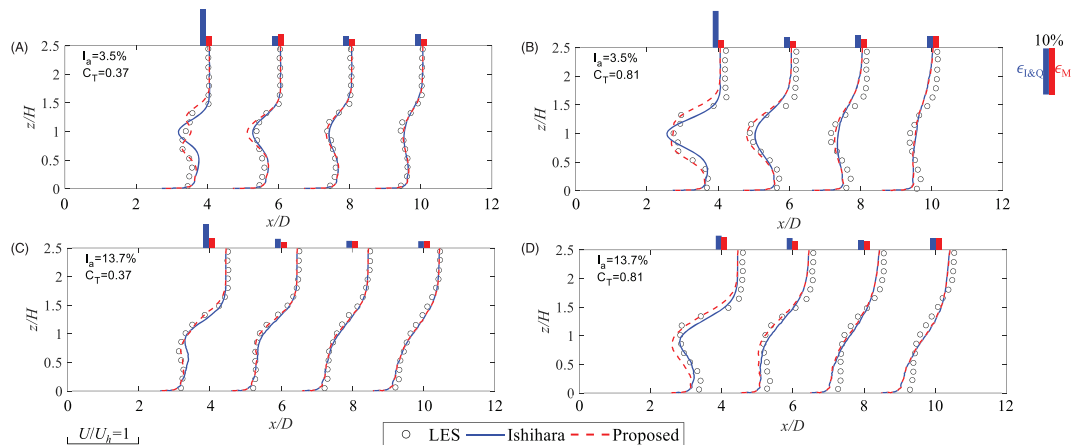| Proposed Model	Parameters
$\frac{\triangle U(x,y,z)}{U_h} = \frac{1}{\left(a + b \cdot \frac{x}{D} + c\left(1 + \frac{x}{D}\right)^{-2}\right)^2}\left(k_1 \times \exp\left(-\frac{(r-m)^2}{1.75\sigma^2}\right) + k_1 \times \exp\left(-\frac{(r+m)^2}{1.75\sigma^2}\right)\right)$	$a = 0.93C_T^{-0.75}I_a^{0.17}$ $b = 0.42C_T^{0.6}I_a^{0.2}$ $c = 0.15C_T^{-0.25}I_a^{-0.7}$ $\sigma = k^*x + \varepsilon D$ $k^* = 0.11C_T^{1.07}I_a^{0.20}$ $\varepsilon = 0.23C_T^{-0.25}I_a^{0.17}$ $m = 0.453\left(\frac{x}{D}\right)^{-2.0}C_T^{-0.1}I_a^{-0.1}$ $k_1 = 0.89x^{-0.25}$

FIGURE 14 Comparisons of the mean streamwise velocities in the vertical direction, when (A) $I_a = 3.5\%$ and $C_T = 0.37$, (B) $I_a = 3.5\%$ and $C_T = 0.81$, (C) $I_a = 13.7\%$ and $C_T = 0.37$, and (D) $I_a = 13.7\%$ and $C_T = 0.81$ [Colour figure can be viewed at wileyonlinelibrary.com]
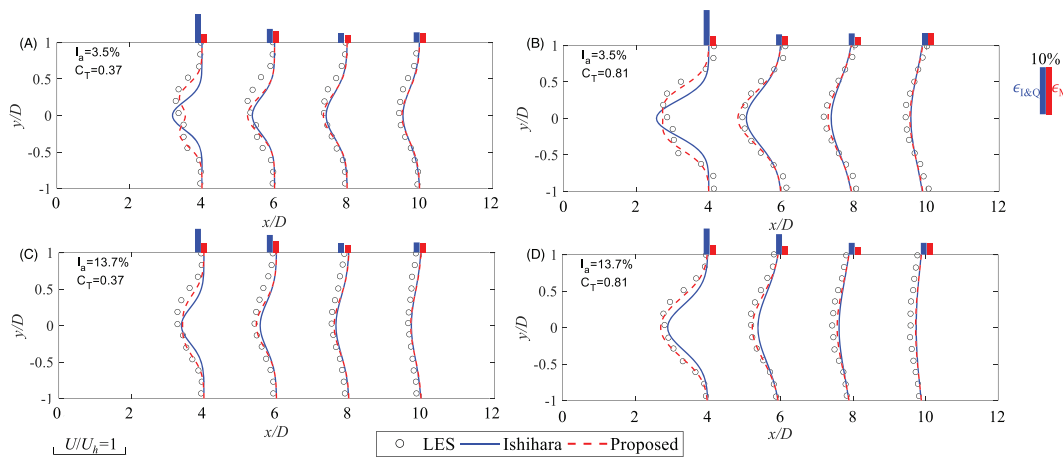
FIGURE 15 Comparisons of the mean streamwise velocities in the horizontal direction, when (A) I_a = 3.5% and C_T = 0.37, (B) I_a = 3.5% and C_T = 0.81, (C) I_a = 13.7% and C_T = 0.37, and (D) I_a = 13.7% and C_T = 0.81 [Colour figure can be viewed at wileyonlinelibrary.com]

U_{LES} is the results from large eddy simulations, N is the sample points in LES. The error bars are added at the top of each profile. From the error bars, it is clear that in the near wake region $x = 2D$, the modified model shows evident improvement in both the vertical and horizontal directions as compared with the original model by Ishihara and Qian.[34]

The mean flow field, as well as the turbulence intensity, can be modeled accurately using the proposed analytical model; however, additional information is still needed to generate the wake flow analytically, ie, the distributions of the integral length scale, spectrum of the velocities, and coherence of the velocities in space. Therefore, more studies considering these issues in turbine wakes are needed to be conducted in the future. Additionally, another important direction is the interaction of turbine wakes.

6 | CONCLUSIONS

In the present study, the ALM model together with LES was employed to obtain the instantaneous flow field in the wake of a wind turbine. A computer code for evaluating the dynamic response of a wind turbine under an arbitrary distribution of the flow field, varying in space and time, was developed. The fatigue load on a downstream wind turbine located at various positions in the wake was examined. To the best of the authors' knowledge, for the first time, the relative effect of the spatial variation of the mean flow field on the fatigue load was clarified. In addition, an analytical model for predicting the mean velocity deficit in both the near-wake and far-wake regions was proposed. Following is a summary of the findings and the contributions from the present study:

1. The flow field predicted by the ALM model together with LES demonstrated satisfactory agreement with the experiments. The developed code for the calculation of the dynamic response of the wind turbine was validated by comparing its results with those of GH-bladed.
2. The averaged bending moments are the smallest when the turbine is located 2D behind the upstream turbine, which are increased as the downstream distance is increased. In addition, the wind turbine in the tandem layout will experience smaller mean bending moments than the corresponding case with a staggered layout.
3. Attributed to the strong wind shear and the large turbulence caused by the upstream wind turbine, the fluctuations of the moments are extraordinarily large in the near-wake region. Moving the wind turbine downstream, the fluctuations of the moments are weakened quickly. And the bending moments at the blade root are more sensitive to the wake-induced flow fields than the tower. The results of the wind turbine in the tandem layout are larger than those in the staggered layout.
4. The EFLs at $x = 2D$ are even 10 times as large as those under the free flow condition. With increasing the distance between the upstream and downstream wind turbines, the EFLs decreases dramatically, and show stable values when $x \geq 6D$.
5. The EFLs determined by the mean flow fields show large values in the near-wake region due to the spatially strong variations of the mean flow. And the results in the staggered layout are larger than those in the tandem layout. In the near-wake region, $x = 2D$, the mean flow contribution to the total EFLs of the wind turbine in the staggered layout can reach to about 85%. Furthermore, as increasing the distance between the wind turbines, the difference between the tandem layout and the staggered layout becomes less obvious.
6. A dual-Gaussian analytical model for predicting the mean velocity deficit was proposed. This model demonstrated obvious improvements in the near-wake region in comparison with the original model. In the far-wake region, both the proposed model and the original model proposed by Ishihara and Qian[34] converged to the same result.

NOMENCLATURE

m_0	total mass of nacelle (kg)
u_J	blade J flapwise displacement (m)
u_T	tower fore-aft displacement (m)
v_J	in-plane displacement for blade J (m)
v_T	in-plane displacement for tower (m)
θ_y	angular displacement at the tower top (°)
Ψ_J	azimuthal angle of blade J (rad)
A	kinety energy (J)
a'	tangential induced factor
ALM	actuator line model
B	number of blades
BEM	blade element method
C_d	drag force coefficient
CFD	computational fluid dynamics
C_l	lift force coefficient
D	diameter of rotor (m)
d	distance to the closest wall (m)
F_D	drag forces (N)
f_i	source term in moment equation (N m^{-3})
F_L	lift forces (N)
FVM	finite volume method
F_x	axial force acting on blade (N)
F_θ	tangential force acting on blade (N)
H	tower height (m)
H_{hub}	hub height (m)
I_a	turbulence intensity of inflow
l	S-N curve slope parameters
LES	large eddy simulation
L_N	equivalent fatigue load
M_{y1}	bending moment at tower base (N m)
M_{y3}	bending moment at blade root (N m)
Q	moment on the blade (N m)
R	blade length (m)
r	distance from blade element to root (m)
s	distance from the tower top to hub (m)
SGS	subgrid scale
SHM	superposition harmonic method
SIMPLE	semi-implicit pressure linked equations
T	thrust on the blade (N)
U	mean streamwise velocity (m s^{-1})
U_∞	free-stream velocity (m s^{-1})
U_h	wind speed at hub height (m s^{-1})
U_r	rated wind speed (m s^{-1})
U_t	total potential energy (J)
V_{rel}	wind velocity relative to the blade (m s^{-1})
x, y, z	coordinates (m)
α	angle of attack (rad)
β	local pitch angle (rad)
λ	tip speed ratio
Λ	volume of a computational cell (m^3)
σ	wake width (m)
σ_u	streamwise fluctuations (m s^{-1})

φ	angle between velocity and rotor plane (rad)
Ω	rotating angular velocity of blade (rad m^{-1})
a	axial-induced factor

ACKNOWLEDGEMENTS

ORCID

Zhenqing Liu (iD) https://orcid.org/0000-0002-3591-334X

REFERENCES

1. Sun H, Yang H. Study on an innovative three-dimensional wind turbine wake model. *Appl Energy*. 2018;226:483-493. https://doi.org/10.1016/j.apenergy.2018.06.027
2. Castellani F, Vignaroli A. An application of the actuator disc model for wind turbine wakes calculations. *Appl Energy*. 2013;101:432-440. https://doi.org/10.1016/j.apenergy.2012.04.039
3. Sedaghatizadeh N, Arjomandi M, Kelso R, Cazzolato B, Ghayesh M. Modelling of wind turbine wake using large eddy simulation. *Renew Energy*. 2018;115:1166-1176. https://doi.org/10.1016/j.renene.2017.09.017
4. Sturge D, Sobotta D, Howell R, While A, Lou J. A hybrid actuator disc–full rotor CFD methodology for modelling the effects of wind turbine wake interactions on performance. *Renew Energy*. 2015;80:525-537. https://doi.org/10.1016/j.renene.2015.02.053
5. Ahmadi M. Influence of upstream turbulence on the wake characteristics of a tidal stream turbine. *Renew Energy*. 2019;132:989-997. https://doi.org/10.1016/j.renene.2018.08.055
6. Chamorro L, Porté-Agel F. A wind-tunnel investigation of wind-turbine wakes: boundary-layer turbulence effects. *Bound-Lay Meteorol*. 2008;132:129-149. https://doi.org/10.1007/s10546-009-9380-8
7. Barthelmie R, Frandsen S, Nielsen N, Pryor S, Rethore P, Jørgensen H. Modelling and measurements of power losses and turbulence intensity in wind turbine wakes at Middelgrunden offshore wind farm. *Wind Energ*. 2007;10(6):517-528. https://doi.org/10.1002/we.238
8. Vera-Tudela L, Kühn M. Analysing wind turbine fatigue load prediction: the impact of wind farm flow conditions. *Renew Energy*. 2017;104:352-360. https://doi.org/10.1016/j.renene.2017.01.065
9. Cosack N. Fatigue load monitoring with standard wind turbine signals. Stuttgart University 2010; Ph. D thesis.
10. Frandsen S, Thøgersen M. Integrated fatigue loading for wind turbines in wind farms by combining ambient turbulence and wakes. *Wind Eng*. 1999;23:327-339. http://www.jstor.org/stable/43749903
11. International Electrotechnical Commission. International Standard IEC 61400–1 Third edition, Wind turbines-part 1: Design requirements, 2005.
12. Thomsen K, Sørensen P. Fatigue loads for wind turbines operating in wakes. *J Wind Eng Ind Aerod*. 1999;80:121-136. https://doi.org/10.1016/S0167-6105(98)00194-9
13. Lee S, Churchfield M, Moriarty P, Jonkman J, Michalakes J. A numerical study of atmospheric and wake turbulence impacts on wind turbine fatigue loadings. 2013;135:31001-31010. https://doi.org/10.1115/1.4023319
14. Kim S, Shin H, Joo Y, Kim K. A study of the wake effects on the wind characteristics and fatigue loads for the turbines in a wind farm. *Renew Energy*. 2015;74:536-543. https://doi.org/10.1016/j.renene.2014.08.054
15. Meng H, Lien F, Li L. Elastic actuator line modelling for wake-induced fatigue analysis of horizontal axis wind turbine blade. *Renew Energy*. 2018;116:423-437. https://doi.org/10.1016/j.renene.2017.08.074
16. Slot R, Sørensen J, Svenningsen L, Moser W, Thøgersen M. Effective turbulence and its implications in wind turbine fatigue assessment. *Wind Energ*. 2019;22:1699-1715. https://doi.org/10.1002/we.2397
17. Holtslag M, Bierbooms W, van Bussel G. Wind turbine fatigue loads as a function of atmospheric conditions offshore. *Wind Energ*. 2016;19:1917-1932. https://doi.org/10.1002/we.1959
18. Nebenführ B, Davidson L. Prediction of wind-turbine fatigue loads in forest regions based on turbulent LES inflow fields. *Wind Energ*. 2017;20:1003-1015. https://doi.org/10.1002/we.2076
19. Zwick D, Muskulus M. Simplified fatigue load assessment in offshore wind turbine structural analysis. *Wind Energ*. 2016;19:265-278. https://doi.org/10.1002/we.1831
20. Dimitrov N, Natarajan A, Kelly M. Model of wind shear conditional on turbulence and its impact on wind turbine loads. *Wind Energ*. 2015;18:1917-1931. https://doi.org/10.1002/we.1797
21. Ciampoli M, Petrini F, Augusti G. Performance-based wind engineering: towards a general procedure. *Struct Saf*. 2011;33(6):367-378. https://doi.org/10.1016/j.strusafe.2011.07.001
22. Larsen C, Madsen H, Thomsen K, Larsen T. Wake meandering: a pragmatic approach. *Wind Energ*. 2008;11:377-395. https://doi.org/10.1002/we.267
23. Keck R, de Maré M, Churchfield M, Lee S, Larsen G, Madsen H. Two improvements to the dynamic wake meandering model: including the effects of atmospheric shear on wake turbulence and incorporating turbulence build-up in a row of wind turbines. *Wind Energ*. 2015;18:111-132. https://doi.org/10.1002/we.1686
24. Larsen T, Madsen H, Larsen G, Hansen K. Validation of the dynamic wake meander model for loads and power production in the Egmond aan zee wind farm. *Wind Energ*. 2013;16:605-624. https://doi.org/10.1002/we.1563
25. Markou H, Andersen P, Larsen G. Potential load reductions on megawatt turbines exposed to wakes using individual-pitch wake compensator and trailing-edge flaps. *Wind Energ*. 2011;14:841-857. https://doi.org/10.1002/we.431
26. Jonkman J, Annoni J, Hayman G, Jonkman B, Purkayastha A. Development of FAST.Farm: a new multi-physics engineering tool for wind-farm design and analysis. 2017; 35th Wind Energy Symposium. Grapevine, United States, https://doi.org/10.2514/6.2017-0454

27. Murtagh P, Ghosh A, Basu B, Broderick B. Passive control of wind turbine vibrations including blade/tower interaction and rotationally sampled turbulence. *Wind Energ*. 2008;11(4):305-317. https://doi.org/10.1002/we.249

28. Jensen N. A note on wind generator interaction. Technical University of Denmark 1983.

29. Katic I, Hojstrup J, Jensen N. A simple model for cluster efficiency. European Wind Energ Conf and Exhib 1986; 407–410.

30. Frandsen S, Barthelmie R, Pryor S, Rathmann O, Larsen S, Hojstrup J. Analytical modelling of wind speed deficit in large offshore wind farms. *Wind Energ*. 2006;9:39-53. https://doi.org/10.1002/we.189

31. Ishihara T, Yamaguchi A, Fujino Y. Development of a new wake model based on a wind tunnel experiment. Global Wind Power 2004.

32. Bastankhah M, Porte-Agel F. A new analytical model for wind-turbine wakes. *Renew Energy*. 2014;70:116-123. https://doi.org/10.1016/j.renene.2014.01.002

33. Gao X, Yang H, Lu L. Optimization of wind turbine layout position in a wind farm using a newly-developed two-dimensional wake model. *Appl Energy*. 2016;174:192-200. https://doi.org/10.1016/j.apenergy.2016.04.098

34. Ishihara T, Qian G. A new Gaussian-based analytical wake model for wind turbines considering ambient turbulence intensities and thrust coefficient effects. *J Wind Eng Ind Aerod*. 2018;177:275-292. https://doi.org/10.1016/j.jweia.2018.04.010

35. Blazek J. *Computational Fluid Dynamics: Principles and Applications*. second ed. Oxford, UK: Elsevier Ltd.; 2005.

36. Martínez-Tossas L, Churchfield M, Leonardi S. Large eddy simulations of the flow past wind turbines: actuator line and disk modeling. *Wind Energ*. 2015;18:1047-1060. https://doi.org/10.1002/we.1747

37. Deskos G, Piggott M. Mesh-adaptive simulations of horizontal-axis turbine arrays using the actuator line method. *Wind Energy*. 2018;21:1266-1281. https://doi.org/10.1002/we.2253

38. Meyer-Forsting A, Pirrung G, Ramos-García N. A vortex-based tip/smearing correction for the actuator line. *Wind Energ Sci Discuss*. 2019;1-22. https://doi.org/10.5194/wes-2018-76

39. Martínez-Tossas L, Churchfield M, Meneveau C. Optimal smoothing length scale for actuator line models of wind turbine blades based on Gaussian body force distribution. *Wind Energ*. 2017;20:1083-1096. https://doi.org/10.1002/we.2081

40. Germanischer L. Rules and regulations: IV - non-marine technology: part 1—wind energy: regulation for the certification of wind energy conversion systems. 1993.

41. Ferziger J, Perić M. *Computational methods for fluid dynamics*. New York: Springer-Verlag; 1996 10.1063/1.881751.

42. Bottasso C, Campagnolo F, Croce A, Dilli S, Gualdoni F, Nielsen M. Structural optimization of wind turbine rotor blades by multilevel sectional/multibody/3D-FEM analysis. *Multibody Syst Dyn*. 2014;32(1):87-116. https://doi.org/10.1007/s11044-013-9394-3

43. Hassan G. Bladed theory manual, 2008; GH report 282/BR/009.

44. Ke S, Wang T, Ge Y, Wang H. Wind-induced fatigue of large HAWT coupled tower–blade structures considering aeroelastic and yaw effects. *Struct Design Tall Spec Build*. 2018;27(9):1467-1478. https://doi.org/10.1002/tal.1467

45. Ke S, Ge Y, Wang T, Cao J, Tamura Y. Wind field simulation and wind-induced responses of large wind turbine tower-blade coupled structure. *Struct Design Tall Spec Build*. 2015;24:571-590. https://doi.org/10.1002/tal.1200

46. Zhang Z, Li J, Nielsen S, Basu B. Mitigation of edgewise vibrations in wind turbine blades by means of roller dampers. *J Sound Vib*. 2014;333(21):5283-5298. https://doi.org/10.1016/j.jsv.2014.06.006

47. Zhang Z. Passive and active vibration control of renewable energy structures. Aalborg University 2015; Ph. D thesis.

48. Jonkman J. The new modularization framework for the FAST wind turbine CAE tool, 51st AIAA aerospace sciences meeting including the new horizons forum and aerospace exposition (AIAA) 2013; grapevine, Texas

49. Branlard ESP. Flexible multibody dynamics using joint coordinates and the Rayleigh-Ritz approximation: the general framework behind and beyond flex. *Wind Energ*. 2019;22:877-893. https://doi.org/10.1002/we.2327

50. Burton T, Jenkins N, Sharpe D, Bossanyi E. *Wind Energy Hsandbook*. West Sussex, UK: Wiley; 2011 10.1002/0470846062.

51. Amzallag C, Gerey J, Robert J, Bahuaud J. Standardization of the rainflow counting method for fatigue analysis. *Int J Fatigue*. 1994;16(4):287-293. https://doi.org/10.1016/0142-1123(94)90343-3

52. Frohboese P, Anders A. Effects of icing on wind turbine fatigue loads. *J Phys: Conference Series*. 2007;75:1-13. https://doi.org/10.1088/1742-6596/75/1/012061

53. Wu Y, Porte-Agel F. Large-eddy simulation of wind-turbine wakes: evaluation of turbine parametrisations. *Bound-Lay Meteorol*. 2011;138:345-366. https://doi.org/10.1007/s10546-010-9569-x

54. Wu Y, Porte-Agel F. Atmospheric turbulence effects on wind-turbine wakes: an LES study. *Energies*. 2012;5:5340-5362. https://doi.org/10.3390/en5125340